

POPULATION III HYPERNOVAE

JOSEPH SMIDT¹, DANIEL J. WHALEN^{1,2}, WESLEY EVEN³, BRANDON WIGGINS⁴, JARRETT L. JOHNSON⁵ AND CHRIS L. FRYER³*Draft version December 3, 2024*

ABSTRACT

Population III supernovae have been of growing interest of late for their potential to directly probe the properties of the first stars, particularly the most energetic events that are visible near the edge of the observable universe. But until now, hypernovae, the unusually energetic Type Ib/c supernovae that are sometimes associated with gamma-ray bursts, have been overlooked as cosmic lighthouses at the highest redshifts. In this, the latest of a series of studies on Population III supernovae, we present numerical simulations of 25 - 50 M_{\odot} hypernovae and their light curves done with the Los Alamos RAGE and SPECTRUM codes. We find that they will be visible at $z = 10 - 15$ to the *James Webb Space Telescope (JWST)* and $z = 4 - 5$ to the Wide-Field Infrared Survey Telescope (WFIRST), tracing star formation rates in the first galaxies and at the end of cosmological reionization. If, however, the hypernova crashes into a dense shell ejected by its progenitor, a superluminous event will occur that may be seen at $z \sim 20$, in the first generation of stars.

Subject headings: early universe – galaxies: high-redshift – galaxies: quasars: general – stars: early-type – supernovae: general – radiative transfer – hydrodynamics – black hole physics – cosmology:theory

1. INTRODUCTION

Population III (Pop III) stars ended the cosmic Dark Ages and began cosmological reionization (e.g., Whalen et al. 2004) and the chemical enrichment of the IGM (Mackey et al. 2003; Smith & Sigurdsson 2007; Smith et al. 2009; Ritter et al. 2012; Safranek-Shrader et al. 2013). They also populated the first galaxies (Johnson et al. 2009; Greif et al. 2010; Jeon et al. 2012; Pawlik et al. 2011; Wise et al. 2012; Pawlik et al. 2013) and may be the origin of supermassive black holes (e.g., Milosavljević et al. 2009; Alvarez et al. 2009; Tanaka & Haiman 2009; Park & Ricotti 2011; Johnson et al. 2012; Whalen & Fryer 2012; Agarwal et al. 2012; Johnson et al. 2013c; Latif et al. 2013a,b). But although they are probably very luminous, individual Pop III stars will not be visible to the *James Webb Space Telescope (JWST)*, Gardner et al. 2006, the Wide-Field Infrared Survey Telescope (WFIRST), or the Thirty-Meter Telescope (TMT; but see Rydberg et al. 2013, about detecting the H II regions of the first stars).

The fossil abundance record (the ashes of early supernovae thought to be imprinted on ancient metal-poor stars, e.g., Beers & Christlieb 2005; Frebel et al. 2005) suggests that some Pop III stars were 15 - 50 M_{\odot} (Joggerst et al. 2010). Numerical simulations of primordial star formation (O’Shea & Norman 2007; Turk et al.

2009; Stacy et al. 2010; Clark et al. 2011; Smith et al. 2011; Greif et al. 2011; Hosokawa et al. 2011; Greif et al. 2012; Stacy et al. 2012; Susa 2013; Hirano et al. 2013) suggest that Pop III stars were 20 - 500 M_{\odot} (for recent reviews, see Whalen 2012; Glover 2013). Together, these studies suggest that both high mass and low mass Pop III stars existed in the primeval universe, but they do not otherwise constrain their properties.

Primordial SNe (e.g., Whalen et al. 2008b) will be the first direct probes of the Pop III initial mass function (IMF) because they can be seen at great distances and the masses of their progenitors can be inferred from their light curves. Recent studies have shown that Pop III pair-instability (PI) SNe (Heger & Woosley 2002; Fryer et al. 2010; Joggerst & Whalen 2011; Kasen et al. 2011; Pan et al. 2012a,b; Hummel et al. 2012; Chatzopoulos & Wheeler 2012; de Souza et al. 2013; Chatzopoulos et al. 2013) will be visible at $z \gtrsim 30$ to deep-field surveys by *JWST* and at $z \sim 15 - 20$ in all-sky near infrared (NIR) surveys by WFIRST and the Wide-Field Imaging Surveyor for High Redshift (WISH) (Whalen et al. 2013a,c,e, 2014; de Souza et al. 2014) (see also Johnson et al. 2013b; Whalen et al. 2013h,g). PI SN candidates have now been identified at low redshifts (Gal-Yam et al. 2009; Cooke et al. 2012) (see also Whalen et al. 2013d). Others have found that *JWST* will detect Pop III core collapse (CC) SNe at $z \sim 10 - 20$, depending on the type of explosion (Whalen et al. 2013b,f,i) (see also Tominaga et al. 2011; Moriya et al. 2013; Tanaka et al. 2012, 2013).

In the past decade, hypernovae (HNe), with energies that are intermediate to those of CC and PI SNe, have been proposed to explain the elemental patterns found in hyper metal-poor stars (e.g., Maeda & Nomoto 2003; Iwamoto et al. 2005; Tominaga et al. 2007) and to account for some unusually bright explosions (e.g.,

¹ T-2, Los Alamos National Laboratory, Los Alamos, NM 87545

² Universität Heidelberg, Zentrum für Astronomie, Institut für Theoretische Astrophysik, Albert-Ueberle-Str. 2, 69120 Heidelberg, Germany

³ CCS-2, Los Alamos National Laboratory, Los Alamos, NM 87545

⁴ Department of Physics and Astronomy, Brigham Young University, Provo, UT 84602

⁵ XTD-6, Los Alamos National Laboratory, Los Alamos, NM 87545

Nomoto et al. 2001; Mazzali et al. 2008). Although HNe are not fully understood, those observed to date have generally been Type Ib/c SNe and have been associated with gamma-ray bursts (GRBs, Iwamoto et al. 1998; Nakamura et al. 2001). They may therefore be the explosions of massive stars that have shed their H envelopes and are bare He cores. The central engine may be a black hole accretion disk system that drives a strong wind or jet that deposits part of its energy into the surrounding layers of the star. The result is a powerful, highly asymmetric explosion that can synthesize large amounts of ^{56}Ni , both of which may account for its brightness. Because their energies typically range from 10 - 50×10^{51} erg, HNe may be visible at redshifts intermediate to those at which PI and CC SNe can be detected. As such, they may be complementary probes of stellar populations in the primordial universe.

We have now calculated light curves and spectra for 25 - 50 M_{\odot} Pop III HNe with the Los Alamos RAGE and SPECTRUM codes. In Section 2 we describe our grid of RAGE models and how we post process them with SPECTRUM to obtain light curves and spectra. In Section 3 we examine blast profiles, and in Section 4 we show NIR light curves and detection thresholds in redshift for HNe. In Section 5 we estimate Pop III HN event rates as a function of redshift, and we conclude in Section 6.

2. NUMERICAL MODELS

We calculate light curves and spectra for HNe in three steps. First, stellar collapse and explosion is modeled in a 1D Lagrangian hydrodynamics code and its output is post processed with an astrophysical nuclear reaction network to obtain nucleosynthetic yields. After explosive burning is complete the blast profiles are ported to the RAGE code and evolved out to one year. We then post process our RAGE profiles with the SPECTRUM code to construct light curves and spectra.

2.1. Collapse and Explosion

To model collapse and explosion, we use the one-dimensional (1D) Lagrangian code and techniques described in Young & Fryer (2007). This code includes three-flavor neutrino transport with flux-limited diffusion and a coupled set of equations of state (EOS) to model the wide range of densities in the collapse phase (for details, see Herant et al. 1994; Fryer et al. 1999a). It includes a 14-element nuclear network (Benz et al. 1989) to follow energy generation. After collapse, bounce and formation of a proto-neutron star, we halt the run and remove the neutron star. To trigger the explosion we inject thermal energy into the innermost 15 zones (roughly $0.035 M_{\odot}$).

The duration and magnitude of the energy injection in these artificial explosions were adjusted to vary the explosion energies. During energy injection, the protoneutron star is modeled as a hard surface. We do not include neutrino flux from the protoneutron star, but the energy injected by this flux is minimal compared to our artificial energy injection. Shortly after the end of the energy injection we change the hard neutron star surface to an absorbing boundary layer to capture the accretion of infalling matter due to neutrino cooling onto the protoneutron star. In this manner we can model the explosion out

to late times, even if there is considerable fallback.

For more accurate yields, we post process our explosions with the public version of the torch code⁶ (Timmes 1999) using the standard 489 isotope network. We explode a 25 M_{\odot} Pop III star with energies of 10, 22, and 52 foe (1 foe = 10^{51} erg) and a 50 M_{\odot} star with energies of 10, 22, 52 and 92 foe. Profiles for these stars are taken from Woosley et al. (2002), and the masses and energies we have chosen bracket those inferred for HNe from observations. We resolve the inner regions of 25 and 50 M_{\odot} stars with 3085 - 3092 zones and 2093 - 2105 zones, respectively.

2.2. RAGE

We evolve the shock out through the surface of the star and into the surrounding medium with the Los Alamos RAGE code (Gittings et al. 2008). RAGE is an adaptive mesh refinement (AMR) radiation hydrodynamics code with a second-order conservative Godunov hydro scheme and grey or multigroup flux-limited diffusion for modeling radiating flows in one, two, or three dimensions (1D, 2D, or 3D). RAGE uses atomic opacities compiled from the OPLIB database⁷ (Magee et al. 1995) and can evolve multimaterial flows with several options of EOS. The physics in our RAGE models is described in Frey et al. (2013): 2-temperature (2T) grey flux-limited diffusion, multispecies advection, and energy deposition due to the radioactive decay of ^{56}Ni (Fryer et al. 2009). We include both the self-gravity of the ejecta and the gravity due to the neutron star or black hole formed in our 1D Lagrangian code. The point mass is initialized with the mass of the remnant plus any additional material that fell back onto it before the model was ported to RAGE. It can continue to grow if there is fallback during the RAGE simulation. Self-gravity must be included to obtain the correct energy and luminosity of the shock because the potential energy of the ejecta at early times is comparable to its kinetic and radiation energies (Whalen et al. 2013a). We evolve mass fractions for H, He, C, N, O, Ne, Mg, Si, S, Ar, Ca, Ti, Cr, Fe and Ni.

2.2.1. Model Setup

Since HNe are associated with Type Ib/c supernovae, we assume that the hydrogen envelope has been stripped from the star prior to the explosion. We therefore port our explosion profiles to RAGE in three stages. First, we map the region from the center of the explosion to the shock in our 1D Lagrangian blast profile onto a uniform 1D spherical mesh in RAGE. We then map the original profile of the star from the radius of the shock to the surface of the He core to the grid. The H layer is discarded, and a wind profile is extended from the surface of the He core out to where its density falls to that of the H II region of the star, as described below. The sharp density drop at the surface of the He core is mitigated by an r^{-20} bridge to the wind to avoid numerical instabilities at shock breakout.

The root grid has 100,000 uniform zones with a resolution of 2×10^6 cm for our 25 M_{\odot} runs and 2×10^7 cm for

⁶ http://cococubed.asu.edu/code_pages/net_torch.shtml

⁷ <http://aphysics2/www.t4.lanl.gov/cgi-bin/opacity/tops.pl>

TABLE 1
HYPERNOVA MODELS (MASSES ARE IN M_{\odot})

M_{\star}	R (10^{10} cm)	E (10^{51} erg)	$M_{56\text{Ni}}$
25	5.3	10	0.035
25	5.3	22	0.080
25	5.3	55	0.166
50	53.7	10	0.498
50	53.7	22	1.405
50	53.7	55	2.726
50	53.7	92	4.06

our 50 M_{\odot} runs. Up to 4 levels of refinement are allowed in the initial interpolation of the profiles onto the setup grid and then during the simulation. We allocate 20 - 25% of this grid to the ejecta profile. The initial radius of the shock varies with explosion energy but is typically about half the radius of the He core. The radius of the inner boundary is the same as in the final output of the 1D Lagrangian model.

We set outflow boundary conditions on the fluid and radiation flows at the inner and outer boundaries of the mesh; the former allows us to tally fallback to the center of the grid and evolve the point mass there. When a run is launched, Courant times are initially short due to high temperatures, large velocities and small cell sizes. To speed up the simulation and accommodate the expansion of the flow we resize the grid by a factor of 2.5 either every 10^6 time steps or when the radiation front has crossed 90% of the grid, whichever happens first. The initial time step on which the new series evolves scales roughly as the ratio of the outer radii of the new and old grids. We again apply up to 4 levels of refinement when mapping the explosion to a new grid and throughout the run thereafter. The properties of our HNe are listed in Table 1.

2.2.2. Circumstellar Envelope

Pop III stars are not generally thought to lose much mass over their lifetimes because there are no line-driven winds in their metal-free atmospheres (Kudritzki 2000; Vink et al. 2001; Baraffe et al. 2001; Ekström et al. 2008). However, they usually do fully ionize their halos and drive out most of the gas, later dying in uniform, low-density H II regions ($n \sim 0.1 - 1 \text{ cm}^{-3}$; e.g., Whalen et al. 2004) (see Whalen & Norman 2008a,b, about the possibility of clumpy circumstellar media). But the processes that strip the H layer from Pop III HN progenitors, such as a common envelope phase with a binary companion or instabilities in the star late in its life (e.g., Fryer & Woosley 1998; Zhang & Fryer 2001; Fryer et al. 2006), reset the density profile in the vicinity of the star. This is true if the star dies in a cosmological halo at $z \sim 20$ or in a protogalaxy at $z \sim 10 - 15$.

The expulsion of the envelope usually proceeds as an outburst that ejects a massive shell that is followed by a fast wind. If the shell is less than ~ 0.01 pc from the star when it dies, ejecta from the HN will crash into it and make a superluminous Type IIn SN (e.g., Moriya et al. 2010, 2013; Whalen et al. 2013b). For simplicity, we assume that the shell has been driven beyond 1 pc so there is no collision and it is too diffuse to attenuate light from the explosion. We thus join a simple low-mass wind pro-

file to the surface of the star:

$$\rho_w(r) = \frac{\dot{m}}{4\pi r^2 v_w}, \quad (1)$$

where \dot{m} is the mass loss rate of the wind and v_w is its speed. We take v_w to be 1000 km s^{-1} and the H and He mass fractions in the wind to be 76% and 24%, respectively. We choose \dot{m} to yield $\rho_w \sim 2 \times 10^{-18} \text{ g cm}^{-3}$ at the bottom of the density bridge from the surface of the star. The wind profile is continued along the grid until its density falls to $n = 0.1 \text{ cm}^{-3}$, that of the H II region of the star. The wind is then replaced by this uniform H II region.

Instead of calculating the ionization state of the wind as in past studies (Whalen & Norman 2006), we take it to be cold ($T = 0.01 \text{ eV}$) and neutral for simplicity. This is probably not true for compact, very hot Type Ic SN progenitors, which ionize their envelopes, so our luminosities should be considered to be lower limits. However, the very diffuse wind envelopes we have chosen are optically thin, so assuming the wind to be neutral is not a serious limitation. We show some initial density and velocity profiles for our RAGE models in Figure 1.

2.3. SPECTRUM

To calculate spectra from a RAGE blast profile we map its densities, temperatures, velocities and mass fractions onto a 2D grid in the Los Alamos SPECTRUM code. SPECTRUM then performs a direct sum of the luminosity of every fluid element in the discretized profile to compute the total flux escaping the ejecta along the line of sight at every wavelength. This procedure accounts for Doppler shifts and time dilation due to the relativistic expansion of the ejecta. SPECTRUM also calculates intensities of emission lines and the attenuation of flux along the line of sight, capturing both limb darkening and absorption lines imprinted on the flux by intervening material in the ejecta and wind. Each spectrum has 14899 wavelengths.

We first extract gas densities, velocities, mass fractions and radiation temperatures from the AMR hierarchy in RAGE and order them by radius in separate files, with one variable per file. Because of constraints on machine memory and time, only a subset of these points are used in SPECTRUM. We determine the position of the radiation front, which is taken to be where aT^4 rises above 10^{-4} erg/cm^3 . Next, we find the radius of the $\tau = 40$ surface by integrating the optical depth due to Thomson scattering in from the outer boundary, taking κ_{Th} to be 0.288 for H and He gas at the mass fractions in the wind (see Section 2.4 of Whalen et al. 2013f). This is the greatest depth from which radiation can escape from the ejecta.

The extracted gas densities, velocities, temperatures and species mass fractions are then interpolated onto a 2D grid in r and θ in SPECTRUM. The inner mesh boundary is the same as in RAGE and the outer boundary is 10^{18} cm . Eight hundred uniform zones in $\log r$ are assigned from the center of the grid to the $\tau = 40$ surface, and the region from the $\tau = 40$ surface to the radiation front is partitioned into 6200 uniform zones in r . The wind between the front and the outer edge of the grid is divided into 500 uniform zones in $\log r$, for a total of

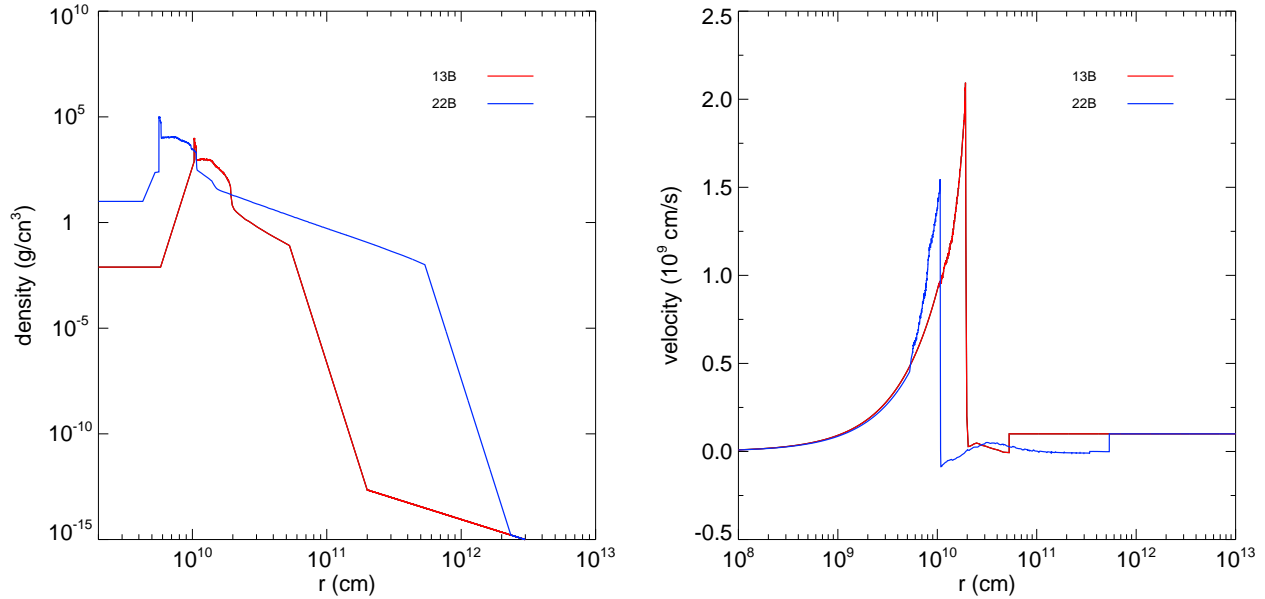


FIG. 1.— Profiles for the shock, the star and its surrounding envelope as initialized in RAGE. Red: 13 foe HN, $25 M_{\odot}$ progenitor. Blue: 22 foe HN, $50 M_{\odot}$ progenitor. Left: densities. Right: velocities.

7500 radial bins. The variables within each of these new radial bins are mass averaged so that the SPECTRUM profile reproduces very sharp features from the RAGE profile. The mesh is uniformly divided into 160 bins in $\mu = \cos \theta$ from -1 to 1. Our grid fully resolves regions of the flow from which photons can escape the ejecta and only lightly samples those from which they cannot.

3. BLAST PROFILES

We show density, temperature and velocity profiles for shock breakout from the star for the 52 foe $50 M_{\odot}$ HN in Figure 2. The shock initially accelerates by a factor of ~ 2.5 in less than 20 seconds, to $\sim 2.4 \times 10^{10} \text{ cm s}^{-1}$, as it descends the density bridge. This acceleration tapers off when it reaches the bottom of the bridge. Radiation breakout coincides with shock breakout. The radiation front (the temperature plateau at 404 and 423 seconds) initially heats the gas to $\sim 200 \text{ eV}$. As the fireball expands, it cools by emitting photons and performing PdV work on the envelope. As it cools, its spectrum softens, and the temperature to which the radiation front heats the surrounding gas also falls.

Naively, one might expect the duration of the breakout transient to be roughly the light crossing time of the star. It is actually longer because photons remain partially coupled to the wispy outer layers of the star that are blown off by the breakout pulse. As they diffuse out through this radiative precursor, they broaden the transient. A few seconds after the precursor is blown off from the shock at ~ 420 seconds, photons escape from its outer layers and become visible to an external observer. As shown in Figure 3, the bolometric luminosity of the breakout transient is $\sim 10^{45} - 10^{47} \text{ erg s}^{-1}$, and is mostly x-rays. Shock breakout happens earlier in the less massive star at a given energy because of its smaller radius. It happens earlier at higher energies because the shock reaches the surface sooner.

Radiation from the shock sustains the radiative pre-

cursor until $\sim 8 \times 10^6$ seconds, as seen in Figure 4. The precursor is visible as the complex structure in velocity and density at $\sim 10^{14} \text{ cm}$ at 9829 seconds. A short-lived reverse shock is visible at $2.0 \times 10^{15} \text{ cm}$ at 3.37e5 seconds, and is gone by 4.7e6 seconds, as shown in Figure 5. The shock eventually overtakes the precursor and merges with it by $\sim 3 \text{ yr}$. The shock overtakes the precursor because it dims as it expands and cools, so its radiative flux can no longer maintain it. The rebrightening in the 22, 52, and 92 foe $50 M_{\odot}$ explosions at $\sim 6 \times 10^6$ seconds happens because the photosphere recedes down to the hot ^{56}Ni layer in the ejecta. It is brighter with more energetic explosions because they synthesize more ^{56}Ni (and it is absent in the least energetic $50 M_{\odot}$ HN and the $25 M_{\odot}$ HNe because they make very little ^{56}Ni). As shown in all three sets of profiles, the expansion of the flow is essentially homologous after 10^7 seconds. All six HNe evolve through these stages in the same manner.

4. NIR LIGHT CURVES / DETECTION LIMITS

In Figures 6-11, we show visible and NIR light curves for all six HNe along with detection limits for current and proposed instruments for $z = 0.01 - 30$. They were obtained from the spectra by summing their luminosities over the appropriate bands and then cosmologically redshifting and dimming them. Since the NIR light curves are all redward of the Lyman limit in the frame of the explosion, we take the transmission coefficient of the neutral IGM at $z \gtrsim 6$ to be 1 (see Figure 3 of de Souza et al. 2013). The detection limits for the Palomar Transient Factory (PTF), the Panoramic Survey Telescope & Rapid Response System (Pan-STARRS) and the Large Synoptic Survey Telescope (LSST) are AB mag 21, 24 and 28, respectively. Photometry limits for *JWST* and WFIRST are AB mag 32 and 27, respectively, which could be extended to 29 for WFIRST with spectrum stacking. Note that wavelengths can be extracted from the *JWST* filter names by dividing their numbers

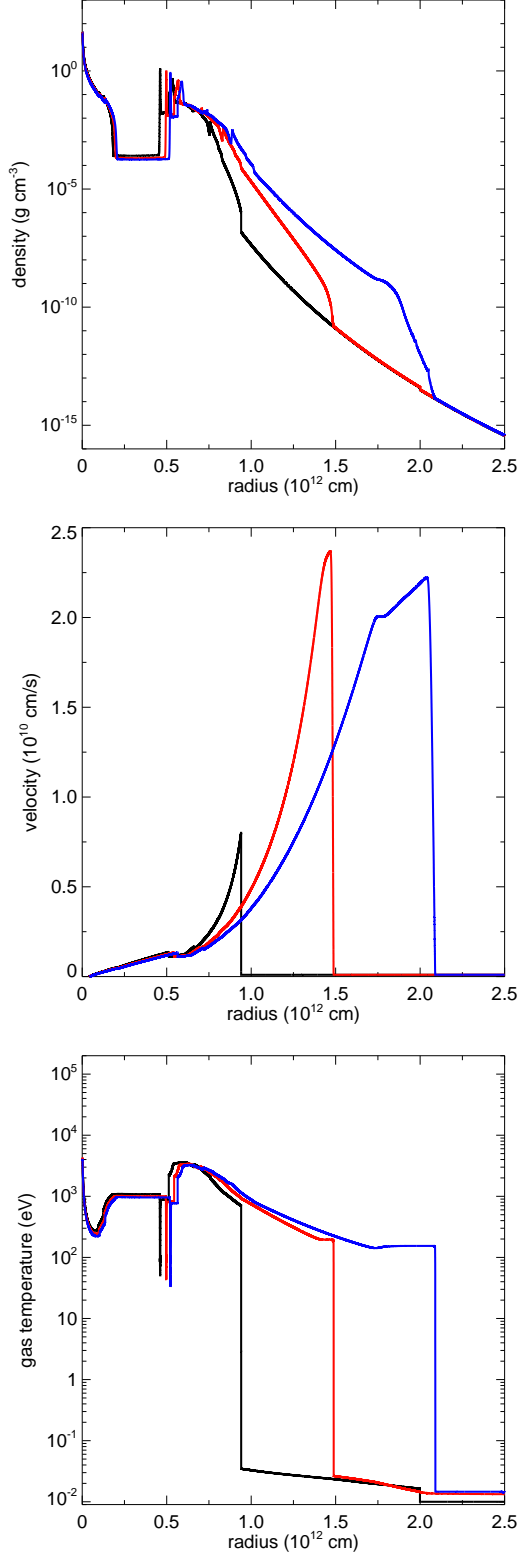


FIG. 2.— Shock breakout for the 52 foe $50 M_{\odot}$ HNe. Top: velocities; center: temperatures; bottom: densities. From left to right the times are 374, 404 and 423 seconds.

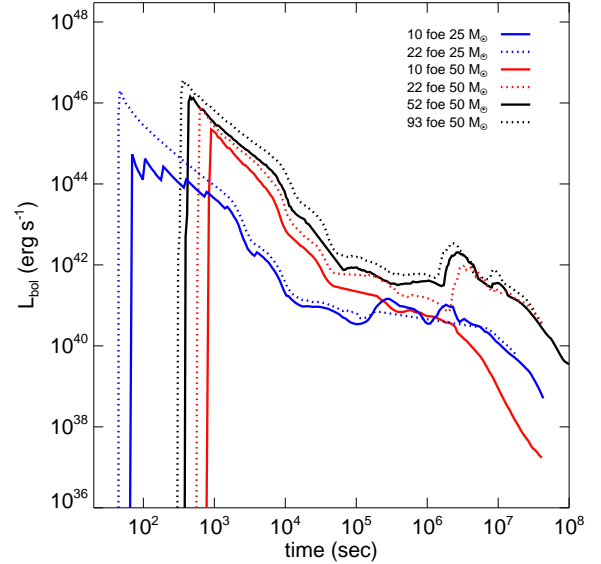


FIG. 3.— Bolometric light curves for all six HNe.

by 100, i.e., the F277W is for $2.77 \mu\text{m}$.

The 22, 52, and 92 foe $50 M_{\odot}$ explosions will be visible to PTF out to $z \sim 0.1$ in the g and r bands from 20 - 80 days, but the 10 foe explosion and the two $25 M_{\odot}$ HNe will only be visible out to $z \sim 0.01$. Pan-STARRS will detect the 52 and 92 foe $50 M_{\odot}$ explosions (and nominally detect the 22 foe HN) out to $z \gtrsim 0.5$ for 10 - 20 days but will only see the others out to $z = 0.1 - 0.4$ for 10 - 100 days. LSST will be able to observe 52 and 92 foe $50 M_{\odot}$ HNe out to $z \sim 2$ for 10 - 40 days, but will only see the others out to $z = 0.5 - 1.5$, depending on explosion energy.

JWST will be able to detect the dimmest events out to $z = 4$ and the more energetic ones out to $z = 10 - 15$. WFIRST could only observe the brightest HNe out to $z \sim 4 - 5$. While *JWST* could therefore detect Pop III HNe in primordial galaxies if it happened across one, WFIRST in principle could see many more of these events because of its large survey areas, but only out to the end of cosmological reionization. Wide survey fields are key to capturing useful numbers of HNe because of their modest event rates, as we discuss in the next section. The fact that these events rise above photometry limits in multiple filters at a given redshift makes it easier to identify them as transients.

5. POP III HN RATES

Pop III HN rates are uncertain because the primordial IMF and star formation rates are unknown. But there is reason to believe that Pop III stars end their lives as HNe at high enough rates to be detected in future surveys. Today, the observed HN rate is within a factor of a few of the GRB rate, which is not surprising given that both are associated with Type Ib/c SNe whose progenitors are probably rapidly-rotating stars with masses $\gtrsim 30 M_{\odot}$ (Podsiadlowski et al. 2004; Guetta & Della Valle 2007). Most Pop III stars are at least this massive, and many of them may be born with high rotation rates (Stacy et al. 2011, 2013; Maeder & Meynet 2012) and die as GRBs or HNe more often than do stars of sim-

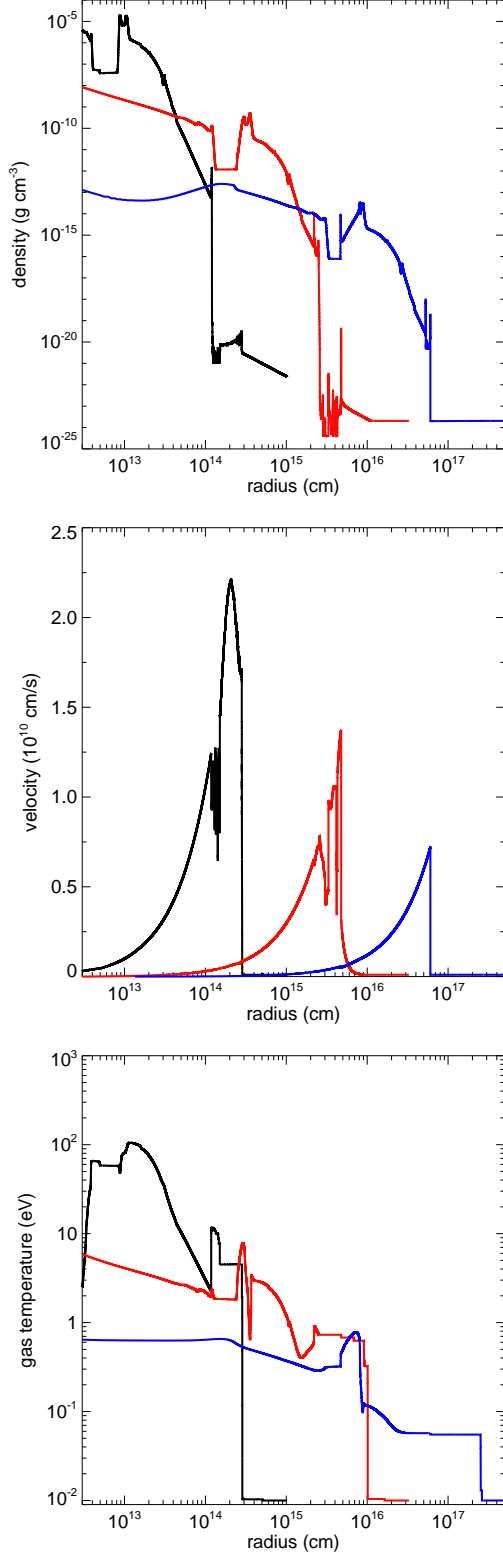


FIG. 4.— Evolution of the 52 foe $50 M_{\odot}$ HN at intermediate times. Top: velocities; center: temperatures; bottom: densities. From left to right the times are 9829, 3.37e5 and 8.38e6 seconds.

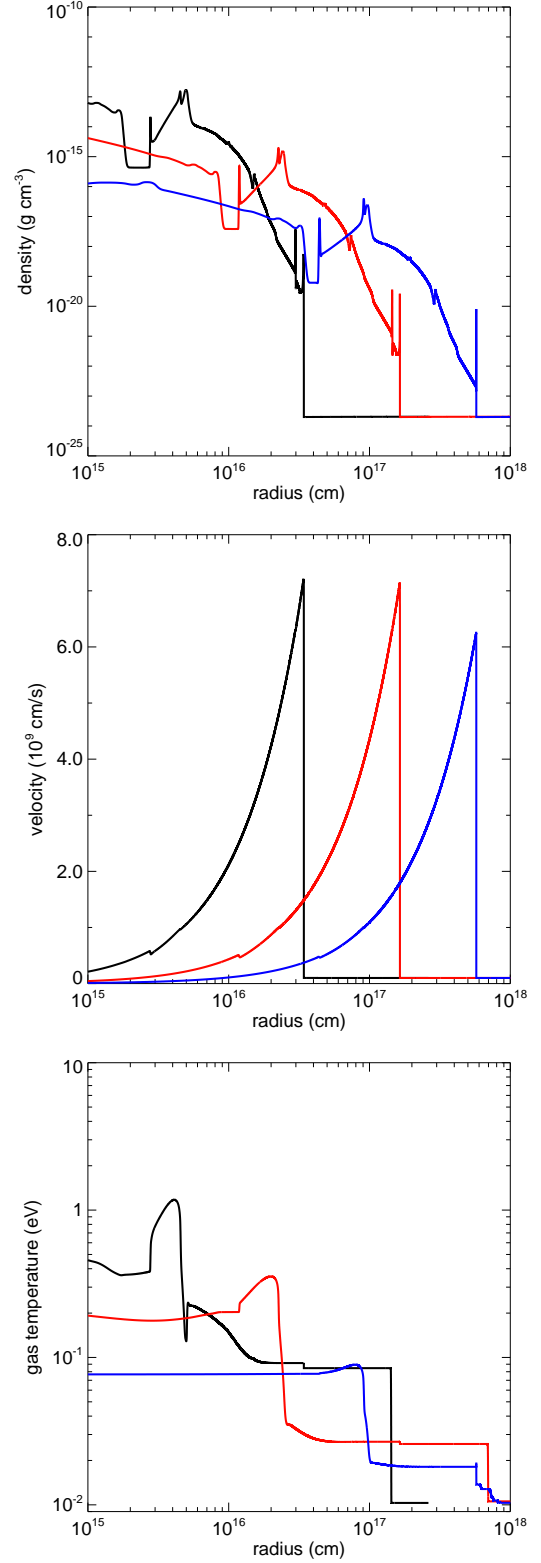


FIG. 5.— Evolution of the 52 foe $50 M_{\odot}$ HN at later times. Top: velocities; center: temperatures; bottom: densities. From left to right the times are 4.7e6, 2.3e7 and 1.0e8 seconds.

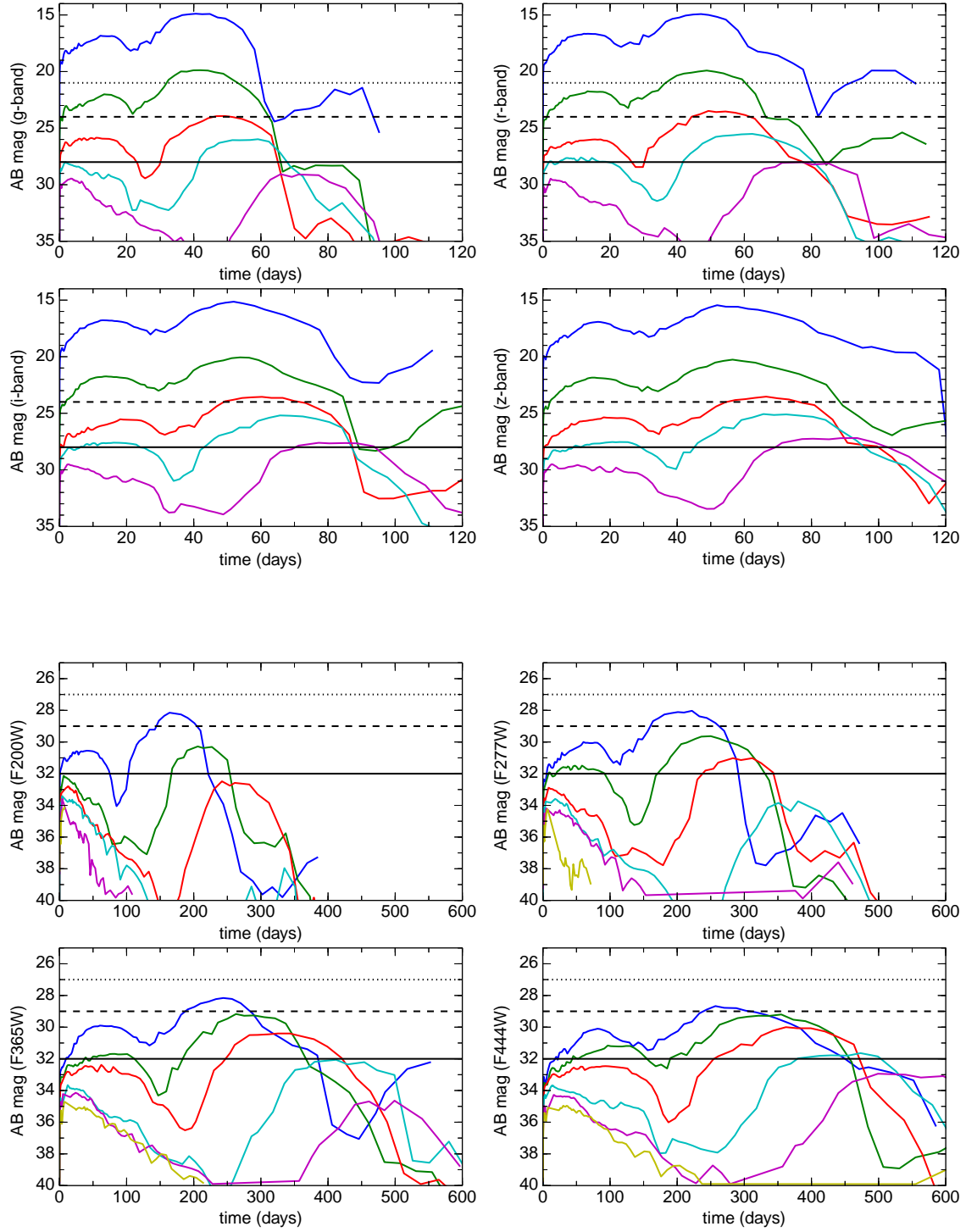


FIG. 6.— Light curves for the 52 foe $50 M_{\odot}$ HN at low redshifts (upper panels) and high redshifts (upper panels). In the upper panels, $z = 0.01$ (dark blue), 0.1 (green), 0.5 (red), 1 (light blue), and 2 (purple). The horizontal dotted, dashed and solid lines are detection limits for PTF, Pan-STARRS and LSST, respectively. In the lower panels, $z = 4$ (dark blue), 7 (green), 10 (red), 15 (light blue), 20 (purple) and 30 (yellow). The horizontal dotted, dashed and solid lines are detection limits for WFIRST, WFIRST with spectrum stacking and *JWST*, respectively.

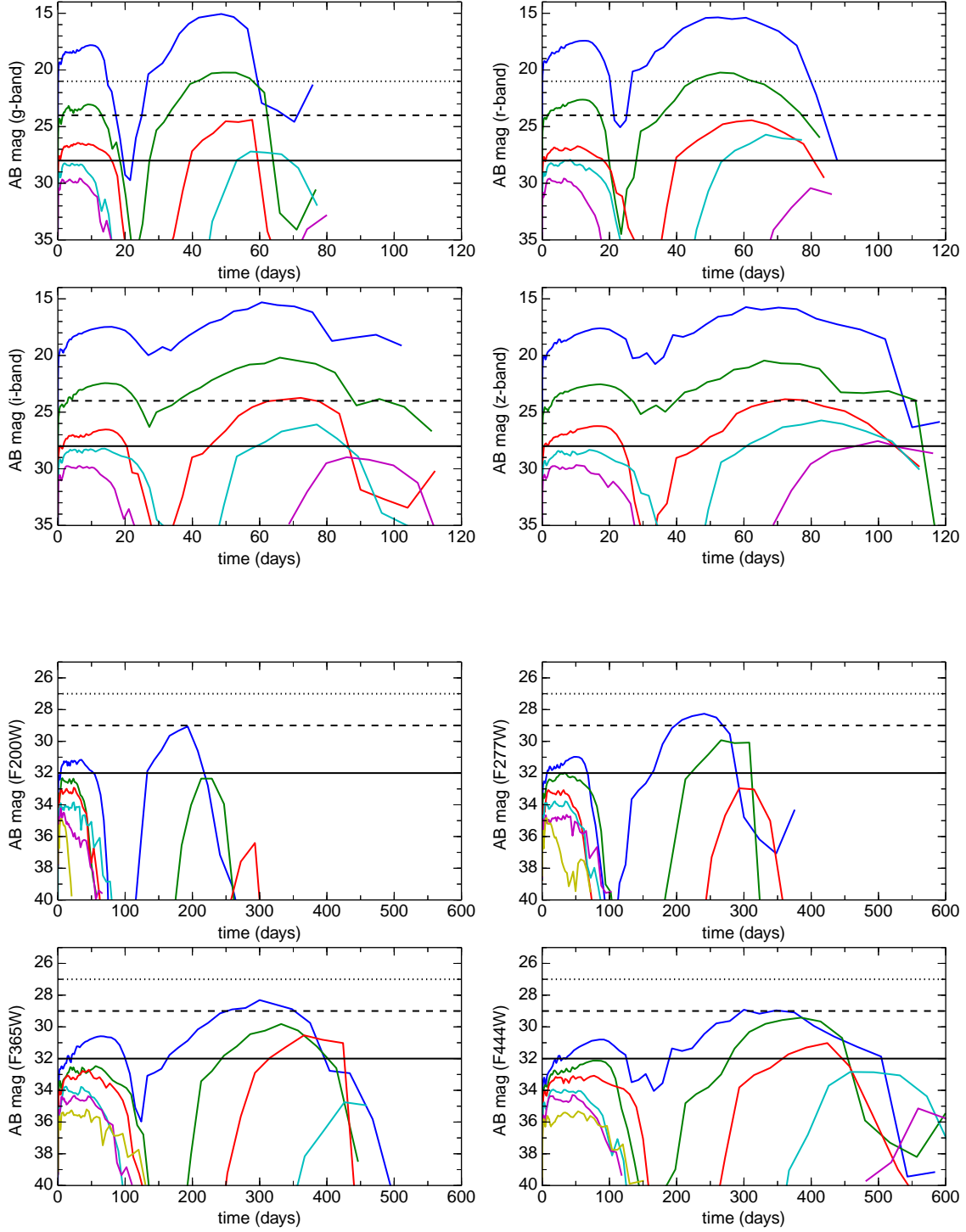


FIG. 7.— Light curves for the 22 foe $50 M_{\odot}$ HN at low redshifts (upper panels) and high redshifts (upper panels). In the upper panels, $z = 0.01$ (dark blue), 0.1 (green), 0.5 (red), 1 (light blue), and 2 (purple). The horizontal dotted, dashed and solid lines are detection limits for PTF, Pan-STARRS and LSST, respectively. In the lower panels, $z = 4$ (dark blue), 7 (green), 10 (red), 15 (light blue), 20 (purple) and 30 (yellow). The horizontal dotted, dashed and solid lines are detection limits for WFIRST, WFIRST with spectrum stacking and JWST, respectively.

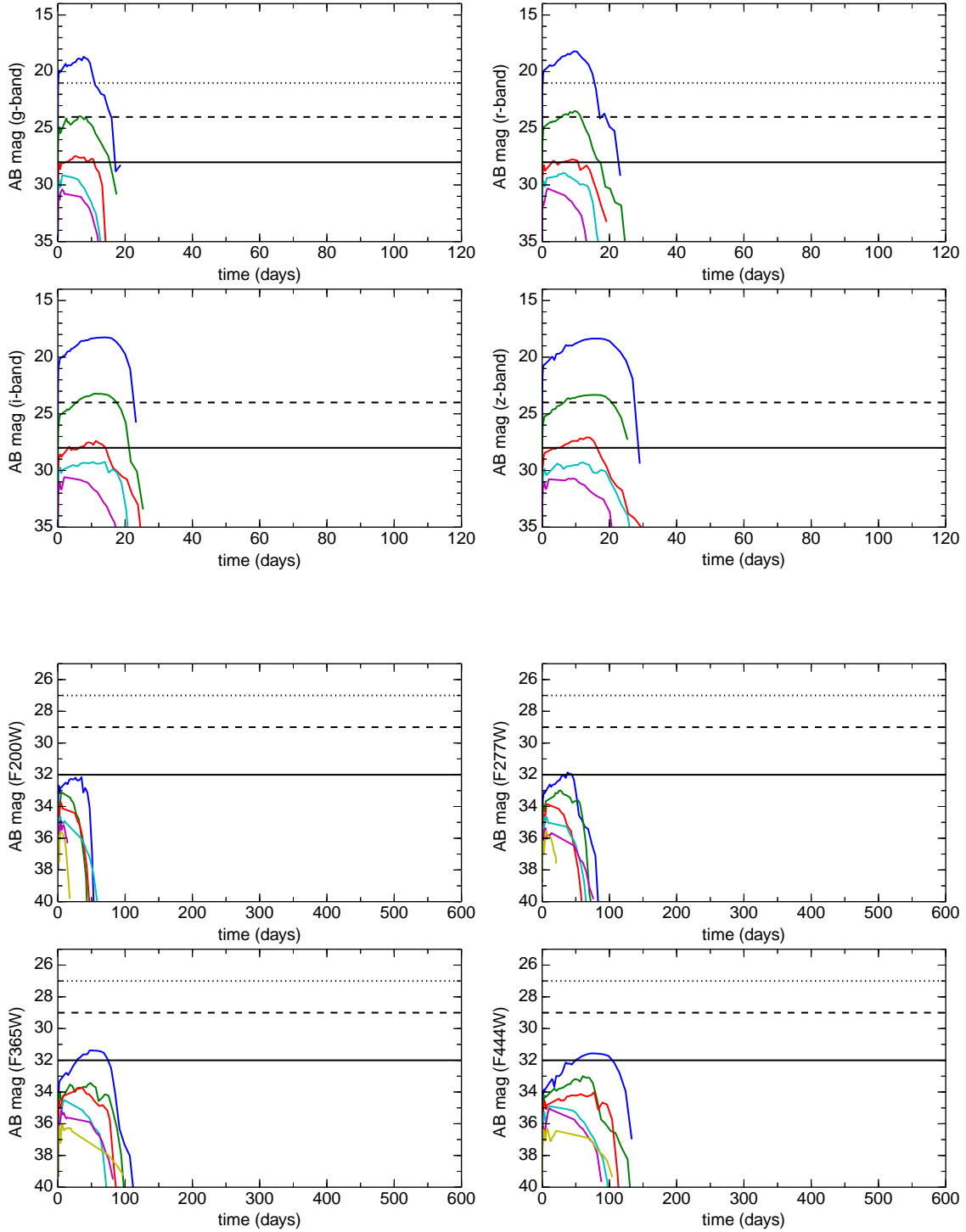


FIG. 8.— Light curves for the 10 foe $50 M_{\odot}$ HN at low redshifts (upper panels) and high redshifts (upper panels). In the upper panels, $z = 0.01$ (dark blue), 0.1 (green), 0.5 (red), 1 (light blue), and 2 (purple). The horizontal dotted, dashed and solid lines are detection limits for PTF, Pan-STARRS and LSST, respectively. In the lower panels, $z = 4$ (dark blue), 7 (green), 10 (red), 15 (light blue), 20 (purple) and 30 (yellow). The horizontal dotted, dashed and solid lines are detection limits for WFIRST, WFIRST with spectrum stacking and JWST, respectively.

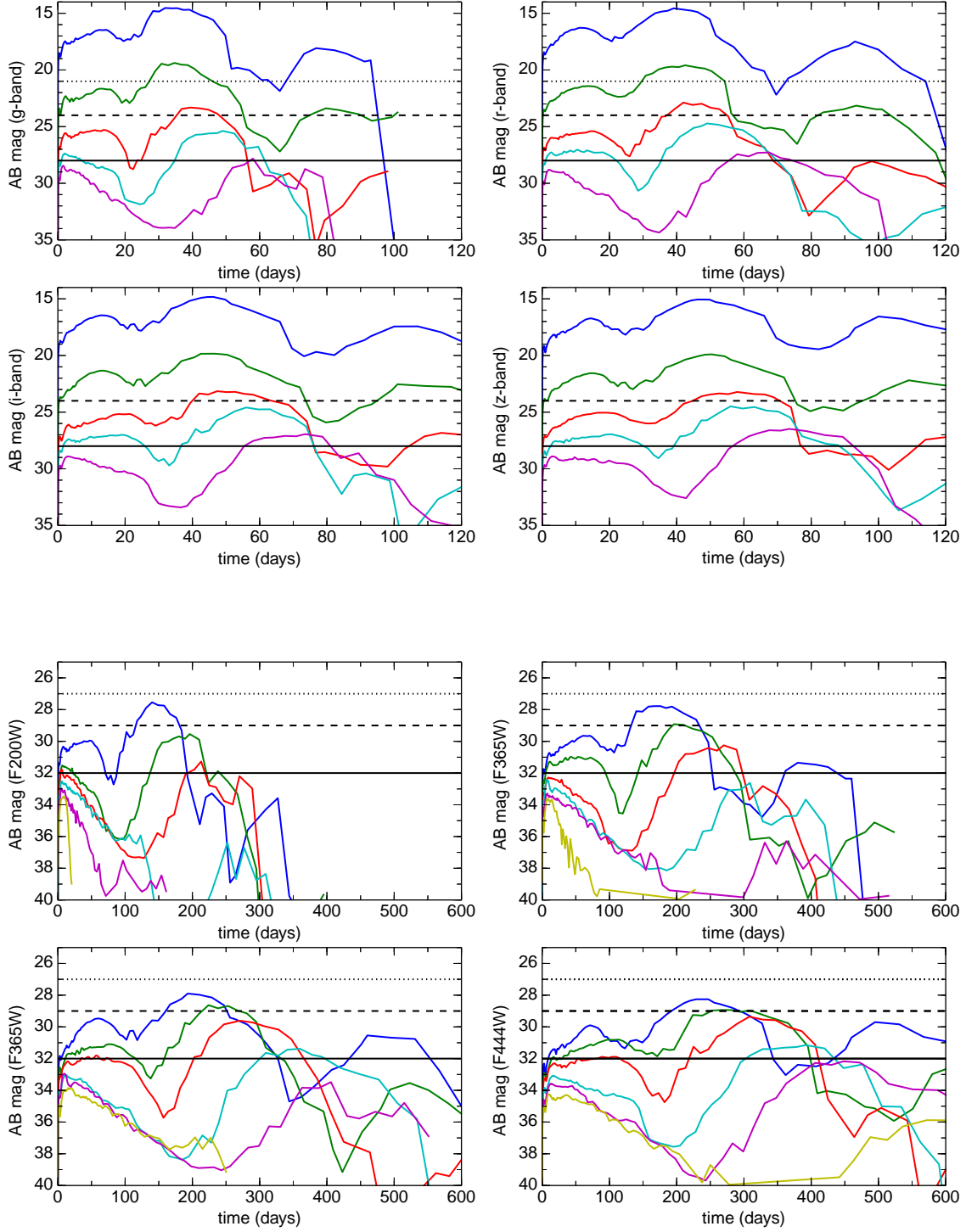


FIG. 9.— Light curves for the 92 foe $50 M_{\odot}$ HN at low redshifts (upper panels) and high redshifts (upper panels). In the upper panels, $z = 0.01$ (dark blue), 0.1 (green), 0.5 (red), 1 (light blue), and 2 (purple). The horizontal dotted, dashed and solid lines are detection limits for PTF, Pan-STARRS and LSST, respectively. In the lower panels, $z = 4$ (dark blue), 7 (green), 10 (red), 15 (light blue), 20 (purple) and 30 (yellow). The horizontal dotted, dashed and solid lines are detection limits for WFIRST, WFIRST with spectrum stacking and JWST, respectively.

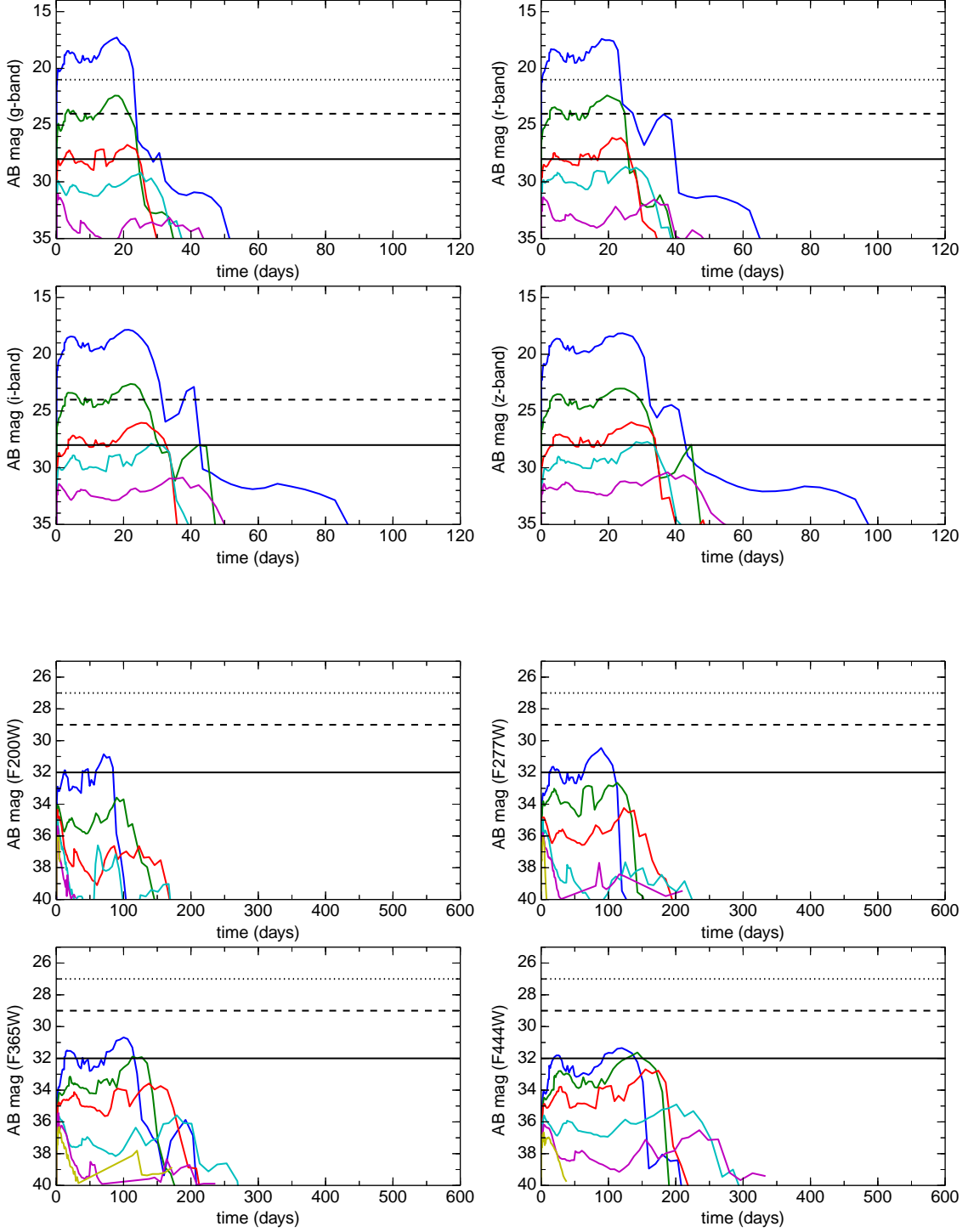


FIG. 10.— Light curves for the 22 foe $25 M_{\odot}$ HN at low redshifts (upper panels) and high redshifts (upper panels). In the upper panels, $z = 0.01$ (dark blue), 0.1 (green), 0.5 (red), 1 (light blue), and 2 (purple). The horizontal dotted, dashed and solid lines are detection limits for PTF, Pan-STARRS and LSST, respectively. In the lower panels, $z = 4$ (dark blue), 7 (green), 10 (red), 15 (light blue), 20 (purple) and 30 (yellow). The horizontal dotted, dashed and solid lines are detection limits for WFIRST, WFIRST with spectrum stacking and JWST, respectively.

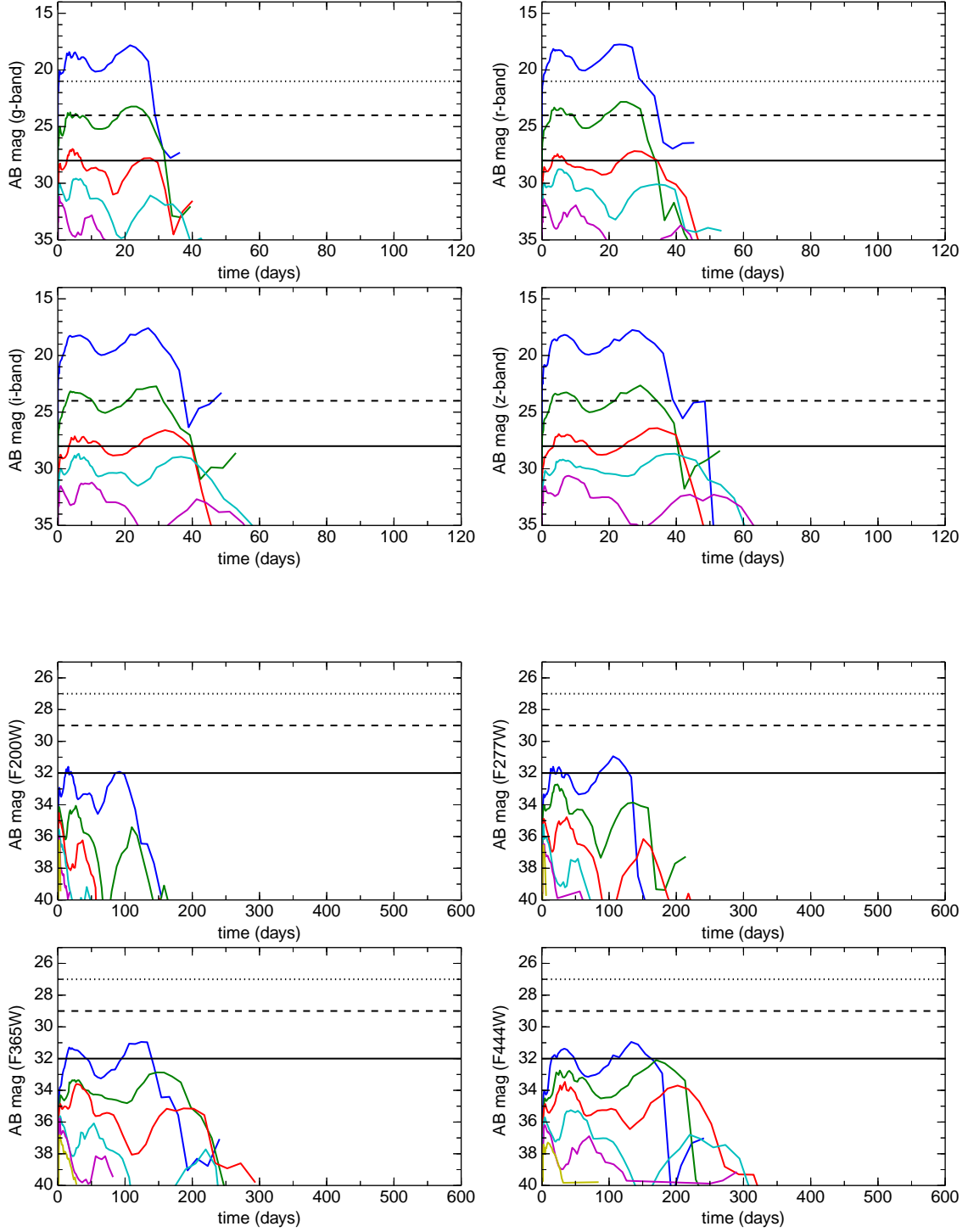


FIG. 11.— Light curves for the 10 foe 25 M_{\odot} HN at low redshifts (upper panels) and high redshifts (upper panels). In the upper panels, $z = 0.01$ (dark blue), 0.1 (green), 0.5 (red), 1 (light blue), and 2 (purple). The horizontal dotted, dashed and solid lines are detection limits for PTF, Pan-STARRS and LSST, respectively. In the lower panels, $z = 4$ (dark blue), 7 (green), 10 (red), 15 (light blue), 20 (purple) and 30 (yellow). The horizontal dotted, dashed and solid lines are detection limits for WFIRST, WFIRST with spectrum stacking and JWST, respectively.

ilar mass today (e.g., Yoon & Langer 2005; Hirschi et al. 2005; Woosley & Heger 2006; Nagakura et al. 2012; Yoon et al. 2012)). There is also evidence that rapidly-rotating Pop III stars (Chiappini et al. 2011) and perhaps HNe (Nomoto et al. 2010) may have synthesized the heavy elements detected in metal-poor stars, which also suggests that HNe may have been common among early stars.

If Pop III HN rates also trace the GRB rate, several recent estimates of the Pop III GRB rate can be used to derive the Pop III HN rate. Bromm & Loeb (2006) predict a total rate of observed Pop III GRBs of $\sim 0.1 \text{ yr}^{-1}$ at $z \gtrsim 15$, which would correspond to $\gtrsim 10 \text{ HNe yr}^{-1}$ if they can be seen at any viewing angle (i.e., if the beaming factor used to calculate the GRB rate is divided out). Distinguishing between Pop III stars that are formed with and without radiative feedback during early galaxy formation, de Souza et al. (2011) predict that GRBs from the former are orders of magnitude more common than those from the latter. They predict an intrinsic GRB rate of $\gtrsim 100 \text{ yr}^{-1}$ out to $z \sim 15$. Campisi et al. (2011) use cosmological simulations of metal enrichment and Pop III and II star formation to place an upper limit of $\sim 1 \text{ yr}^{-1}$ on the observed Pop III GRB rate at $z > 6$, or about 100 HNe yr^{-1} .

Even if no connection is assumed for Pop III GRBs and HNe, an upper limit to the HN rate can be gleaned from cosmological simulations of Pop III star formation that include chemical and radiative feedback (Johnson et al. 2013a) by assuming that all $25 - 140 M_{\odot}$ Pop III stars can produce black holes and HNe (e.g., Fryer 1999; Heger et al. 2003). Assuming a Salpeter-like IMF for primordial stars and a lower mass limit of $21 M_{\odot}$, Johnson et al. (2013a) find a total HN rate of $\sim 10^4 \text{ yr}^{-1}$, with most occurring at $z \lesssim 10$. This rate is broadly consistent with the estimates above if the actual ratio of Pop III black hole-producing SNe to Pop III HNe is similar to the observed ratio today (~ 100 ; Podsiadlowski et al. 2004). We conclude that HNe could occur at rates of $\gtrsim 10 \text{ yr}^{-1}$, and perhaps up to $\gtrsim 100 \text{ yr}^{-1}$, at $z \lesssim 15$.

6. CONCLUSION

Pop III HNe will be visible in the NIR out to $z \sim 10 - 15$ by *JWST* and out to $z \sim 4 - 5$ to WFIRST and WISH. This picture changes if the progenitor ejects a massive shell and the HN crashes into it. Such collisions can produce superluminous supernovae (SLSNe) like SN 2006gy (Smith et al. 2007; Moriya et al. 2010; Chevalier & Irwin 2011; Moriya et al. 2013) that would be brighter than the HN itself. The high luminosities of SLSNe are due to the large radius of the shell upon impact. Much less energetic Pop III Type II_n SNe (2 foe) can be detected by *JWST* at $z \sim 15 - 20$ and WFIRST at $z \sim 7$ (Whalen et al. 2013b), suggesting that HNe that collide with dense shells may be visible to all-sky NIR missions like WFIRST out to $z \sim 10 - 15$. This would greatly enhance their prospects for detection, since the

large survey areas of these missions could compensate for low HN rates. We are now modeling these events with RAGE.

If most Pop III HNe are associated with GRBs, and most GRBs are due to binary mergers with companion stars (e.g., Fryer & Woosley 1998; Fryer et al. 1999b; Zhang & Fryer 2001; Fryer et al. 2007), then there is additional reason to believe HNe may have been common in the primordial universe because Pop III stars have now been found to form in binaries and small multiples in simulations (Turk et al. 2009; Stacy et al. 2010). The GRBs themselves might be detected by other means. Gamma rays from these events could trigger *Swift* or its successors, such as the Joint Astrophysics Nascent Universe Satellite (JANUS, Mészáros & Rees 2010; Roming 2008; Burrows et al. 2010), and their afterglows (Whalen et al. 2008a) might be found in all-sky radio surveys by the Extended Very Large Array (eVLA), eMERLIN and the Square Kilometer Array (SKA) (de Souza et al. 2011) (see also Suwa & Ioka 2011; Nagakura et al. 2012). It is now known that Pop III GRB afterglows will be bright enough in the NIR to be seen *JWST*, WFIRST, and the TMT (Mesler et al. 2012, 2013) (and that they would completely outshine the HN).

Could later stages of HNe be detected in other ways? Whalen et al. (2008b) found that most of the kinetic energy of $40 M_{\odot}$ Pop III HNe is eventually radiated away as H and He lines in primordial halos as the remnant sweeps up and shocks gas. This emission is too diffuse, redshifted and extended over time to be detected by any upcoming instruments. Also, unlike Pop III PI SNe, HNe do not inject enough energy into the cosmic microwave background (CMB) to impose excess power on the CMB at small scales (Oh et al. 2003; Whalen et al. 2008b) or be directly imaged by the Atacama Cosmology Telescope or the South Pole Telescope via the Sunyaev-Zeldovich effect. But new calculations reveal that enough synchrotron emission from their remnants would redshifted into the radio above $z \sim 10$ to be directly detected by current facilities such as eVLA and eMERLIN and by SKA (Meiksin & Whalen 2013). Whether in the NIR, radio, or in the fossil abundance record, these ancient explosions could soon open another window on the $z \sim 10 - 15$ universe.

JS and JLJ were supported by LANL LDRD Director's Fellowships. DJW was supported from the Baden-Württemberg-Stiftung by contract research via the programme Internationale Spitzenforschung II (grant P-LS-SPII/18). Work at LANL was done under the auspices of the National Nuclear Security Administration of the U.S. Department of Energy at Los Alamos National Laboratory under Contract No. DE-AC52-06NA25396. All CASTRO, RAGE and SPECTRUM calculations were performed on Institutional Computing (IC) and Yellow network platforms at LANL (Pinto, Mustang and Moonlight).

REFERENCES

- Agarwal, B., Khochfar, S., Johnson, J. L., Neistein, E., Dalla Vecchia, C., & Livio, M. 2012, MNRAS, 425, 2854
- Alvarez, M. A., Wise, J. H., & Abel, T. 2009, ApJ, 701, L133
- Baraffe, I., Heger, A., & Woosley, S. E. 2001, ApJ, 550, 890
- Beers, T. C. & Christlieb, N. 2005, ARA&A, 43, 531
- Benz, W., Thielemann, F.-K., & Hills, J. G. 1989, ApJ, 342, 986
- Bromm, V. & Loeb, A. 2006, ApJ, 642, 382

- Burrows, D. N., Roming, P. W. A., Fox, D. B., Herter, T. L., Falcone, A., Bilén, S., Nousek, J. A., & Kennea, J. A. 2010, in Presented at the Society of Photo-Optical Instrumentation Engineers (SPIE) Conference, Vol. 7732, Society of Photo-Optical Instrumentation Engineers (SPIE) Conference Series
- Campisi, M. A., Maio, U., Salvaterra, R., & Ciardi, B. 2011, *MNRAS*, 416, 2760
- Chatzopoulos, E. & Wheeler, J. C. 2012, *ApJ*, 748, 42
- Chatzopoulos, E., Wheeler, J. C., & Couch, S. M. 2013, *ApJ*, 776, 129
- Chevalier, R. A. & Irwin, C. M. 2011, *ApJ*, 729, L6+
- Chiappini, C., Frischknecht, U., Meynet, G., Hirschi, R., Barbay, B., Pignatari, M., Decressin, T., & Maeder, A. 2011, *Nature*, 474, 666
- Clark, P. C., Glover, S. C. O., Smith, R. J., Greif, T. H., Klessen, R. S., & Bromm, V. 2011, *Science*, 331, 1040
- Cooke, J., Sullivan, M., Gal-Yam, A., Barton, E. J., Carlberg, R. G., Ryan-Weber, E. V., Horst, C., Omori, Y., & Díaz, C. G. 2012, *Nature*, 491, 228
- de Souza, R. S., Ishida, E. E. O., Johnson, J. L., Whalen, D. J., & Mesinger, A. 2013, *MNRAS*, 436, 1555
- de Souza, R. S., Ishida, E. E. O., Whalen, D. J., Johnson, J., & Ferrara, A. 2014, arXiv:1401.2995
- de Souza, R. S., Yoshida, N., & Ioka, K. 2011, *A&A*, 533, A32
- Ekström, S., Meynet, G., Chiappini, C., Hirschi, R., & Maeder, A. 2008, *A&A*, 489, 685
- Frebel, A., Aoki, W., Christlieb, N., Ando, H., Asplund, M., Barklem, P. S., Beers, T. C., Eriksson, K., Fechner, C., Fujimoto, M. Y., Honda, S., Kajino, T., Minezaki, T., Nomoto, K., Norris, J. E., Ryan, S. G., Takada-Hidai, M., Tsangarides, S., & Yoshii, Y. 2005, *Nature*, 434, 871
- Frey, L. H., Even, W., Whalen, D. J., Fryer, C. L., Hungerford, A. L., Fontes, C. J., & Colgan, J. 2013, *ApJS*, 204, 16
- Fryer, C., Benz, W., Herant, M., & Colgate, S. A. 1999a, *ApJ*, 516, 892
- Fryer, C. L. 1999, *ApJ*, 522, 413
- Fryer, C. L., Brown, P. J., Bufano, F., Dahl, J. A., Fontes, C. J., Frey, L. H., Holland, S. T., Hungerford, A. L., Immler, S., Mazzali, P., Milne, P. A., Scannapieco, E., Weinberg, N., & Young, P. A. 2009, *ApJ*, 707, 193
- Fryer, C. L., Mazzali, P. A., Prochaska, J., Cappellaro, E., Panaitescu, A., Berger, E., van Putten, M., van den Heuvel, E. P. J., Young, P., Hungerford, A., Rockefeller, G., Yoon, S.-C., Podsiadlowski, P., Nomoto, K., Chevalier, R., Schmidt, B., & Kulkarni, S. 2007, *PASP*, 119, 1211
- Fryer, C. L., Rockefeller, G., & Young, P. A. 2006, *ApJ*, 647, 1269
- Fryer, C. L., Whalen, D. J., & Frey, L. 2010, in American Institute of Physics Conference Series, Vol. 1294, American Institute of Physics Conference Series, ed. D. J. Whalen, V. Bromm, & N. Yoshida, 70–75
- Fryer, C. L. & Woosley, S. E. 1998, *ApJ*, 502, L9
- Fryer, C. L., Woosley, S. E., & Hartmann, D. H. 1999b, *ApJ*, 526, 152
- Gal-Yam, A., Mazzali, P., Ofek, E. O., Nugent, P. E., Kulkarni, S. R., Kasliwal, M. M., Quimby, R. M., Filippenko, A. V., Cenko, S. B., Chornock, R., Waldman, R., Kasen, D., Sullivan, M., Beshore, E. C., Drake, A. J., Thomas, R. C., Bloom, J. S., Poznanski, D., Miller, A. A., Foley, R. J., Silverman, J. M., Arcavi, I., Ellis, R. S., & Deng, J. 2009, *Nature*, 462, 624
- Gardner, J. P., Mather, J. C., Clampin, M., Doyon, R., Greenhouse, M. A., Hammel, H. B., Hutchings, J. B., Jakobsen, P., Lilly, S. J., Long, K. S., Lunine, J. I., McCaughrean, M. J., Mountain, M., Nella, J., Rieke, G. H., Rieke, M. J., Rix, H.-W., Smith, E. P., Sonneborn, G., Stiavelli, M., Stockman, H. S., Windhorst, R. A., & Wright, G. S. 2006, *Space Sci. Rev.*, 123, 485
- Gittings, M., Weaver, R., Clover, M., Betlach, T., Byrne, N., Coker, R., Dendy, E., Hueckstaedt, R., New, K., Oakes, W. R., Ranta, D., & Stefan, R. 2008, *Computational Science and Discovery*, 1, 015005
- Glover, S. 2013, in *Astrophysics and Space Science Library*, Vol. 396, *Astrophysics and Space Science Library*, ed. T. Wiklund, B. Mobasher, & V. Bromm, 103
- Greif, T. H., Bromm, V., Clark, P. C., Glover, S. C. O., Smith, R. J., Klessen, R. S., Yoshida, N., & Springel, V. 2012, *MNRAS*, 424, 399
- Greif, T. H., Glover, S. C. O., Bromm, V., & Klessen, R. S. 2010, *ApJ*, 716, 510
- Greif, T. H., Springel, V., White, S. D. M., Glover, S. C. O., Clark, P. C., Smith, R. J., Klessen, R. S., & Bromm, V. 2011, *ApJ*, 737, 75
- Guetta, D. & Della Valle, M. 2007, *ApJ*, 657, L73
- Heger, A., Fryer, C. L., Woosley, S. E., Langer, N., & Hartmann, D. H. 2003, *ApJ*, 591, 288
- Heger, A. & Woosley, S. E. 2002, *ApJ*, 567, 532
- Herant, M., Benz, W., Hix, W. R., Fryer, C. L., & Colgate, S. A. 1994, *ApJ*, 435, 339
- Hirano, S., Hosokawa, T., Yoshida, N., Umeda, H., Omukai, K., Chiaki, G., & Yorke, H. W. 2013, arXiv:1308.4456
- Hirschi, R., Meynet, G., & Maeder, A. 2005, *A&A*, 443, 581
- Hosokawa, T., Omukai, K., Yoshida, N., & Yorke, H. W. 2011, *Science*, 334, 1250
- Hummel, J. A., Pawlik, A. H., Milosavljević, M., & Bromm, V. 2012, *ApJ*, 755, 72
- Iwamoto, K., Mazzali, P. A., Nomoto, K., Umeda, H., Nakamura, T., Patat, F., Danziger, I. J., Young, T. R., Suzuki, T., Shigeyama, T., Augusteijn, T., Doublier, V., Gonzalez, J.-F., Boehnhardt, H., Brewer, J., Hainaut, O. R., Lidman, C., Leibundgut, B., Cappellaro, E., Turatto, M., Galama, T. J., Vreeswijk, P. M., Kouveliotou, C., van Paradijs, J., Pian, E., Palazzi, E., & Frontera, F. 1998, *Nature*, 395, 672
- Iwamoto, N., Umeda, H., Tominaga, N., Nomoto, K., & Maeda, K. 2005, *Science*, 309, 451
- Jeon, M., Pawlik, A. H., Greif, T. H., Glover, S. C. O., Bromm, V., Milosavljević, M., & Klessen, R. S. 2012, *ApJ*, 754, 34
- Joggerst, C. C., Almgren, A., Bell, J., Heger, A., Whalen, D., & Woosley, S. E. 2010, *ApJ*, 709, 11
- Joggerst, C. C. & Whalen, D. J. 2011, *ApJ*, 728, 129
- Johnson, J. L., Dalla, V. C., & Khochfar, S. 2013a, *MNRAS*, 428, 1857
- Johnson, J. L., Greif, T. H., Bromm, V., Klessen, R. S., & Ippolito, J. 2009, *MNRAS*, 399, 37
- Johnson, J. L., Whalen, D. J., Even, W., Fryer, C. L., Heger, A., Smidt, J., & Chen, K.-J. 2013b, arXiv:1304.4601
- Johnson, J. L., Whalen, D. J., Fryer, C. L., & Li, H. 2012, *ApJ*, 750, 66
- Johnson, J. L., Whalen, D. J., Li, H., & Holz, D. E. 2013c, *ApJ*, 771, 116
- Kasen, D., Woosley, S. E., & Heger, A. 2011, *ApJ*, 734, 102
- Kudritzki, R. 2000, in *The First Stars*, ed. A. Weiss, T. G. Abel, & V. Hill, 127–+
- Latif, M. A., Schleicher, D. R. G., Schmidt, W., & Niemeyer, J. 2013a, *MNRAS*, 433, 1607
- . 2013b, *MNRAS*, 430, 588
- Mackey, J., Bromm, V., & Hernquist, L. 2003, *ApJ*, 586, 1
- Maeda, K. & Nomoto, K. 2003, *ApJ*, 598, 1163
- Maeder, A. & Meynet, G. 2012, *Reviews of Modern Physics*, 84, 25
- Magee, N. H., Abdallah, Jr., J., Clark, R. E. H., Cohen, J. S., Collins, L. A., Csanak, G., Fontes, C. J., Gauger, A., Keady, J. J., Kilcrease, D. P., & Merts, A. L. 1995, in *Astronomical Society of the Pacific Conference Series*, Vol. 78, *Astrophysical Applications of Powerful New Databases*, ed. S. J. Adelman & W. L. Wiese, 51
- Mazzali, P. A., Valenti, S., Della Valle, M., Chincarini, G., Sauer, D. N., Benetti, S., Pian, E., Piran, T., D’Elia, V., Elias-Rosa, N., Margutti, R., Pasotti, F., Antonelli, L. A., Bufano, F., Campana, S., Cappellaro, E., Covino, S., D’Avanzo, P., Fiore, F., Fugazza, D., Gilmozzi, R., Hunter, D., Maguire, K., Maiorano, E., Marziani, P., Masetti, N., Mirabel, F., Navasardyan, H., Nomoto, K., Palazzi, E., Pastorello, A., Panagia, N., Pellizza, L. J., Sari, R., Smartt, S., Tagliaferri, G., Tanaka, M., Taubenberger, S., Tominaga, N., Trundle, C., & Turatto, M. 2008, *Science*, 321, 1185
- Meiksin, A. & Whalen, D. J. 2013, *MNRAS*, 430, 2854
- Mesler, R. A., Whalen, D. J., Lloyd-Ronning, N. M., Fryer, C. L., & Pihlström, Y. M. 2012, *ApJ*, 757, 117
- . 2013, *ApJ*, in prep
- Mészáros, P. & Rees, M. J. 2010, *ApJ*, 715, 967
- Milosavljević, M., Bromm, V., Couch, S. M., & Oh, S. P. 2009, *ApJ*, 698, 766

- Moriya, T., Yoshida, N., Tominaga, N., Blinnikov, S. I., Maeda, K., Tanaka, M., & Nomoto, K. 2010, in *American Institute of Physics Conference Series*, Vol. 1294, American Institute of Physics Conference Series, ed. D. J. Whalen, V. Bromm, & N. Yoshida, 268–269
- Moriya, T. J., Blinnikov, S. I., Tominaga, N., Yoshida, N., Tanaka, M., Maeda, K., & Nomoto, K. 2013, *MNRAS*, 428, 1020
- Nagakura, H., Suwa, Y., & Ioka, K. 2012, *ApJ*, 754, 85
- Nakamura, T., Mazzali, P. A., Nomoto, K., & Iwamoto, K. 2001, *ApJ*, 550, 991
- Nomoto, K., Mazzali, P. A., Nakamura, T., Iwamoto, K., Danziger, I. J., & Patat, F. 2001, in *Supernovae and Gamma-Ray Bursts: the Greatest Explosions since the Big Bang*, ed. M. Livio, N. Panagia, & K. Sahu, 144–170
- Nomoto, K., Tanaka, M., Tominaga, N., & Maeda, K. 2010, *New Astronomy Reviews*, 54, 191
- Oh, S. P., Cooray, A., & Kamionkowski, M. 2003, *MNRAS*, 342, L20
- O’Shea, B. W. & Norman, M. L. 2007, *ApJ*, 654, 66
- Pan, T., Kasen, D., & Loeb, A. 2012a, *MNRAS*, 422, 2701
- Pan, T., Loeb, A., & Kasen, D. 2012b, *MNRAS*, 423, 2203
- Park, K. & Ricotti, M. 2011, *ApJ*, 739, 2
- Pawlik, A. H., Milosavljević, M., & Bromm, V. 2011, *ApJ*, 731, 54
- , 2013, *ApJ*, 767, 59
- Podsiadlowski, P., Mazzali, P. A., Nomoto, K., Lazzati, D., & Cappellaro, E. 2004, *ApJ*, 607, L17
- Ritter, J. S., Safrank-Shrader, C., Gnat, O., Milosavljević, M., & Bromm, V. 2012, *ApJ*, 761, 56
- Roming, P. 2008, in *COSPAR, Plenary Meeting*, Vol. 37, 37th COSPAR Scientific Assembly, 2645–+
- Rydberg, C.-E., Zackrisson, E., Lundqvist, P., & Scott, P. 2013, *MNRAS*, 429, 3658
- Safrank-Shrader, C., Milosavljevic, M., & Bromm, V. 2013, *arXiv:1307.1982*
- Smith, B. D. & Sigurdsson, S. 2007, *ApJ*, 661, L5
- Smith, B. D., Turk, M. J., Sigurdsson, S., O’Shea, B. W., & Norman, M. L. 2009, *ApJ*, 691, 441
- Smith, N., Li, W., Foley, R. J., Wheeler, J. C., Pooley, D., Chornock, R., Filippenko, A. V., Silverman, J. M., Quimby, R., Bloom, J. S., & Hansen, C. 2007, *ApJ*, 666, 1116
- Smith, R. J., Glover, S. C. O., Clark, P. C., Greif, T., & Klessen, R. S. 2011, *MNRAS*, 414, 3633
- Stacy, A., Bromm, V., & Loeb, A. 2011, *MNRAS*, 413, 543
- Stacy, A., Greif, T. H., & Bromm, V. 2010, *MNRAS*, 403, 45
- , 2012, *MNRAS*, 422, 290
- Stacy, A., Greif, T. H., Klessen, R. S., Bromm, V., & Loeb, A. 2013, *MNRAS*, 431, 1470
- Susa, H. 2013, *ApJ*, 773, 185
- Suwa, Y. & Ioka, K. 2011, *ApJ*, 726, 107
- Tanaka, M., Moriya, T. J., & Yoshida, N. 2013, *arXiv:1306.3743*
- Tanaka, M., Moriya, T. J., Yoshida, N., & Nomoto, K. 2012, *MNRAS*, 422, 2675
- Tanaka, T. & Haiman, Z. 2009, *ApJ*, 696, 1798
- Timmes, F. X. 1999, *ApJS*, 124, 241
- Tominaga, N., Morokuma, T., Blinnikov, S. I., Baklanov, P., Sorokina, E. I., & Nomoto, K. 2011, *ApJS*, 193, 20
- Tominaga, N., Umeda, H., & Nomoto, K. 2007, *ApJ*, 660, 516
- Turk, M. J., Abel, T., & O’Shea, B. 2009, *Science*, 325, 601
- Vink, J. S., de Koter, A., & Lamers, H. J. G. L. M. 2001, *A&A*, 369, 574
- Whalen, D., Abel, T., & Norman, M. L. 2004, *ApJ*, 610, 14
- Whalen, D. & Norman, M. L. 2006, *ApJS*, 162, 281
- , 2008a, *ApJ*, 673, 664
- Whalen, D., Prochaska, J. X., Heger, A., & Tumlinson, J. 2008a, *ApJ*, 682, 1114
- Whalen, D., van Veelen, B., O’Shea, B. W., & Norman, M. L. 2008b, *ApJ*, 682, 49
- Whalen, D. J. 2012, *arXiv:1209.4688*
- Whalen, D. J., Even, W., Frey, L. H., Smidt, J., Johnson, J. L., Lovekin, C. C., Fryer, C. L., Stiavelli, M., Holz, D. E., Heger, A., Woosley, S. E., & Hungerford, A. L. 2013a, *ApJ*, 777, 110
- Whalen, D. J., Even, W., Lovekin, C. C., Fryer, C. L., Stiavelli, M., Roming, P. W. A., Cooke, J., Pritchard, T. A., Holz, D. E., & Knight, C. 2013b, *ApJ*, 768, 195
- Whalen, D. J., Even, W., Smidt, J., Heger, A., Chen, K.-J., Fryer, C. L., Stiavelli, M., Xu, H., & Joggerst, C. C. 2013c, *ApJ*, 778, 17
- Whalen, D. J., Even, W., Smidt, J., Heger, A., Hirschi, R., Yusof, N., Stiavelli, M., Fryer, C. L., Chen, K.-J., & Joggerst, C. C. 2013d, *arXiv:1312.5360*
- Whalen, D. J. & Fryer, C. L. 2012, *ApJ*, 756, L19
- Whalen, D. J., Fryer, C. L., Holz, D. E., Heger, A., Woosley, S. E., Stiavelli, M., Even, W., & Frey, L. H. 2013e, *ApJ*, 762, L6
- Whalen, D. J., Joggerst, C. C., Fryer, C. L., Stiavelli, M., Heger, A., & Holz, D. E. 2013f, *ApJ*, 768, 95
- Whalen, D. J., Johnson, J. L., Smidt, J., Heger, A., Even, W., & Fryer, C. L. 2013g, *ApJ*, 777, 99
- Whalen, D. J., Johnson, J. L., Smidt, J., Meiksin, A., Heger, A., Even, W., & Fryer, C. L. 2013h, *ApJ*, 774, 64
- Whalen, D. J. & Norman, M. L. 2008b, *ApJ*, 672, 287
- Whalen, D. J., Smidt, J., Even, W., Woosley, S. E., Heger, A., Stiavelli, M., & Fryer, C. L. 2014, *ApJ*, 781, 106
- Whalen, D. J., Smidt, J., Johnson, J. L., Holz, D. E., Stiavelli, M., & Fryer, C. L. 2013i, *arXiv:1312.6330*
- Wise, J. H., Turk, M. J., Norman, M. L., & Abel, T. 2012, *ApJ*, 745, 50
- Woosley, S. E. & Heger, A. 2006, *ApJ*, 637, 914
- Woosley, S. E., Heger, A., & Weaver, T. A. 2002, *Reviews of Modern Physics*, 74, 1015
- Yoon, S.-C., Dierks, A., & Langer, N. 2012, *A&A*, 542, A113
- Yoon, S.-C. & Langer, N. 2005, *A&A*, 443, 643
- Young, P. A. & Fryer, C. L. 2007, *ApJ*, 664, 1033
- Zhang, W. & Fryer, C. L. 2001, *ApJ*, 550, 357